JOURNAL OF
APPLIED
CRYSTALLOGRAPHY

Volume 55 (2022)

Supporting information for article:

Quick and robust PDF data acquisition using laboratory single-crystal X-ray diffractometer for study of polynuclear lanthanide complexes in solid and in solution

Dmitry Tsymbarenko, Dimitry Grebenyuk, Maria Burlakova and Mirijam Zobel

S1. Pair Distribution Function

Total scattering structure function $S(Q)$ is obtained as follows:

$$S(Q)=\frac{I_c(Q)-\langle f(Q)^2\rangle+\langle f(Q)\rangle^2}{\langle f(Q)\rangle^2} \tag{1}$$

where $I_c(Q)$ is the coherent scattering, $f(Q)$ is the atomic scattering vector. Angle brackets indicate an average over all atom types in the sample.

$S(Q)$ can be transformed into the PDF, $G(r)$, by Fourier transform as follows (Farrow & Billinge, 2009):

$$G(r)=\frac{2}{\pi}\int_{Q_{min}}^{Q_{max}} Q\left[S(Q)-1\right]\sin(Qr)\,dQ=\frac{2}{\pi}\int_{Q_{min}}^{Q_{max}} F(Q)\sin(Qr)\,dQ \tag{2}$$

where $F(Q) = Q[S(Q)-1]$ is the reduced structure function (Warren, 1990).

S2. Data collection strategy

To optimize sample-to-detector distance the distances were tested: 59 mm – the shortest possible distance for QUEST diffractometer, 100 mm – intermediate distance, and 200 mm – longest reasonable distance. The series of frames with the step of 5º were collected for each distance in $2\theta_D$ range of 0-120º (25 frames) or 0-115º (24 frames for 59 mm due to hardware limit). Profiles were obtained by integration of frame series by FormagiX software. The comparison of resulted profiles (Fig. S1) reveals the detector distance of 100 mm to be the optimal. It gives the spatial resolution (FWHM the most intense peak of LaB_6 is as low as 0.285º which is equal to beam divergence of 5 mrad = 0.287º). The longest sample-to-detector distance, 200 mm, does not improve the resolution (peak FWHM remains unchanged) but significantly reduces the collected intensities due to geometrical factor and reduces the maximum available Q value. The shortest sample-to-detector distance, 59 mm, increases the maximum available Q value to 17.3 $Å^{-1}$ but it dramatically decreases the resolution (peak FWHM is 0.53º). This makes the resulted PDF for 59 mm much worse than for 100 mm (Fig. S2). Namely, peak magnitudes show significant decay beyond 40 Å, and after 60 Å PDF consists almost only of Fourier ripples. At the same time the PDF for 100 mm shows reasonable peaks even at 140 Å.

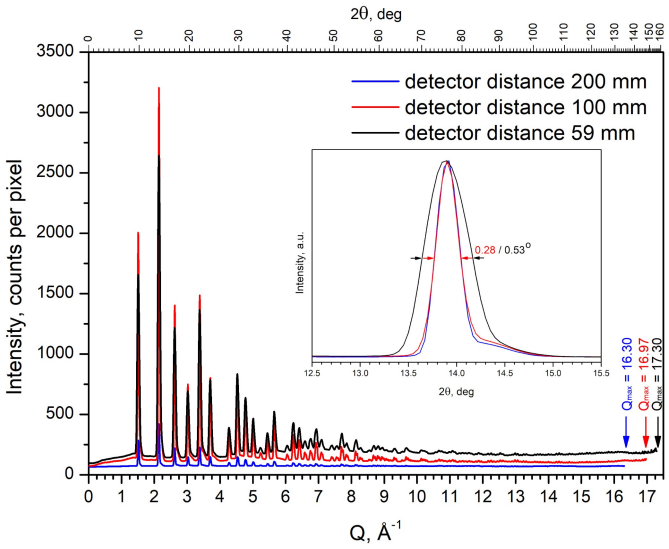

Figure S1 Experimental $I(Q)$ profiles of NIST SRM660 LaB_6 powder collected at different sample-to-detector distances (59, 100 and 200 mm). Inset shows the $I(2\theta)$ profiles of the most intense LaB_6 peak scaled to equal maxima, arrows show the peak FWHM.

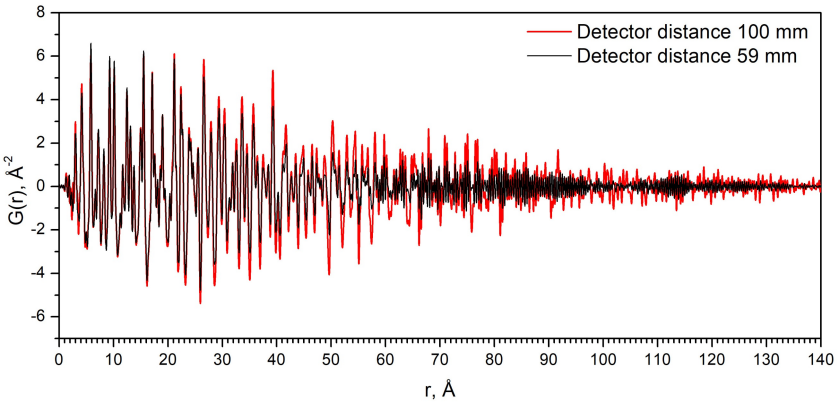

Figure S2 Experimental PDF of LaB_6 powder calculated from scattering data collected at 59- and 100-mm sample-to-detector distances. Q_{max} was set equal to 16.97 Å^{-1} for both cases.

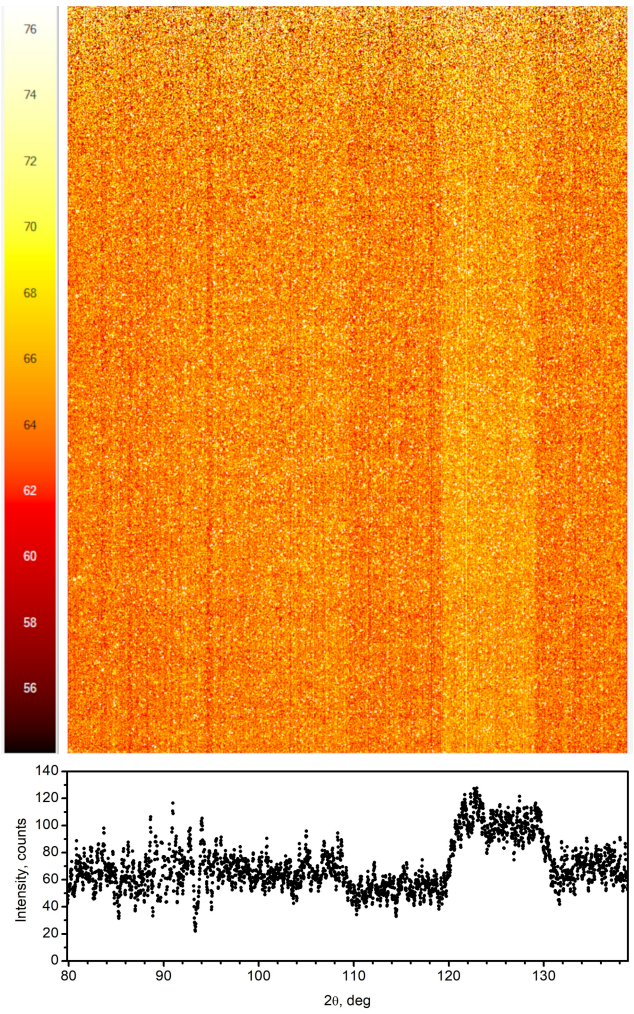

Figure S3 Frame collected with no sample (air scattering) at detector $2\theta_D$ position 110º, detector distance 90 mm, Exposure time 60 sec. Chips rows are clearly visible. The intensity vs 2θ angle was obtained by azimuthal integration within Bruker APEX4 package.

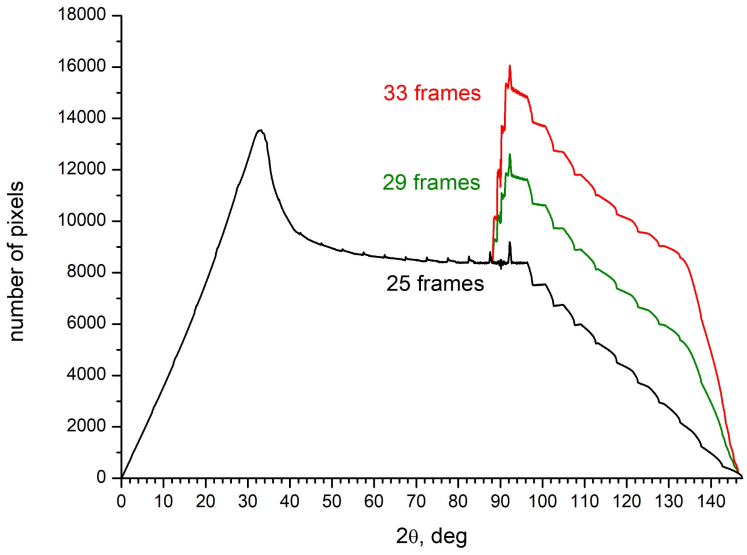

Figure S4 Number of detector pixels contributing to resulting $I(2\theta)$ at a particular 2θ angle after azimuthal integration and merging of all frames. $\Delta 2\theta$ step equals to 0.05º.

Table S1 Details of data collection strategy.

Frame number	Strategy					
	25 Frames		**29 Frames**		**33 Frames**	
	$2\theta_D$,°	ω,°	$2\theta_D$,°	ω,°	$2\theta_D$,°	ω,°
1	0	0.0	0	0.0	0	0.0
2	5	2.5	5	2.5	5	2.5
3	10	5.0	10	5.0	10	5.0
4	15	7.5	15	7.5	15	7.5
5	20	10.0	20	10.0	20	10.0
6	25	12.5	25	12.5	25	12.5
7	30	15.0	30	15.0	30	15.0
8	35	17.5	35	17.5	35	17.5
9	40	20.0	40	20.0	40	20.0
10	45	22.5	45	22.5	45	22.5
11	50	25.0	50	25.0	50	25.0
12	55	27.5	55	27.5	55	27.5
13	60	30.0	60	30.0	60	30.0
14	65	32.5	65	32.5	65	32.5
15	70	35.0	70	35.0	70	35.0
16	75	37.5	75	37.5	75	37.5
17	80	40.0	80	40.0	80	40.0
18	85	42.5	85	42.5	85	42.5
19	90	45.0	90	45.0	90	45.0
20	95	47.5	95	47.5	95	47.5
21	100	50.0	100	50.0	100	50.0
22	105	52.5	105	52.5	105	52.5
23	110	55.0	110	55.0	110	55.0
24	115	57.5	115	57.5	115	57.5
25	120	60.0	116	58.0	116	58.0
26			117	58.5	116	58.0
27			118	59.0	117	58.5
28			119	59.5	117	58.5
29			120	60.0	118	59.0
30					118	59.0
31					119	59.5
32					119	59.5
33					120	60.0

S3. Data reduction

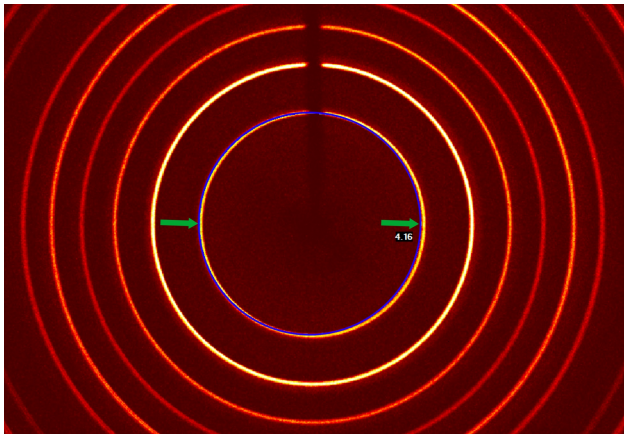

Figure S5 Fragment of experimental Frame of NIST LaB_6 powder acquired for 60 sec at detector $2\theta_D$ position equals to 0º, detector distance 100mm. Blue circle is the expected position of the first Debye ring of LaB_6 (d-spacing 4.158 Å) calculated for the pre-defined detector parameters (stored in the frame header). Green arrows point on areas with the most pronounced misalignment effects.

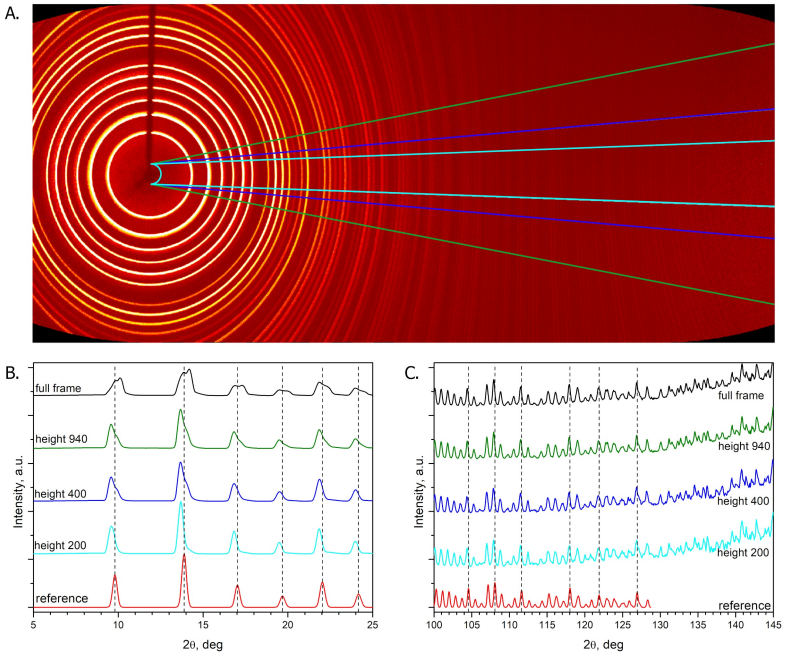

Figure S6 Integration of powder LaB_6 frames by Bruker APEX4 software: merged cylindrical projection of frames with indicated height-limited regions used for integration (A); integrated profiles in a comparison with reference pattern of LaB_6 in small-angle (B) and large-angle (C) ranges, the intensities of large-angle were multiplied by factor 100 for clarity. The height-limited integration is performed within Slice Tool for regions with max height of 200 pixels (cyan lines, ca. 11% of full frame), 400 pixels (blue lines, 19% of full frame) and 940 pixels (green lines, 35% of full frame). Full frame integration is done with the Wedge Tool. Reference pattern of LaB_6 (red lines) is generated based on structural data of LaB_6 and cell parameters taken from NIST SRM660 Certificate. Dash lines show the position of selected peaks of LaB_6 standard.

S4. Data analysis by Rietveld method and PDF for reference samples

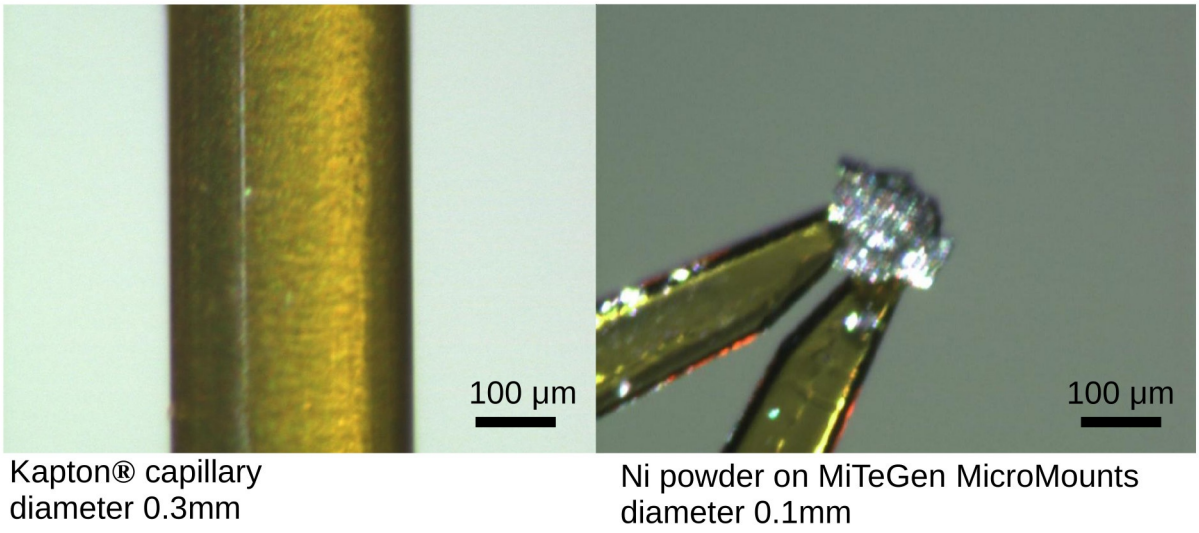

Figure S7 Photographs of samples prepared for measurements.

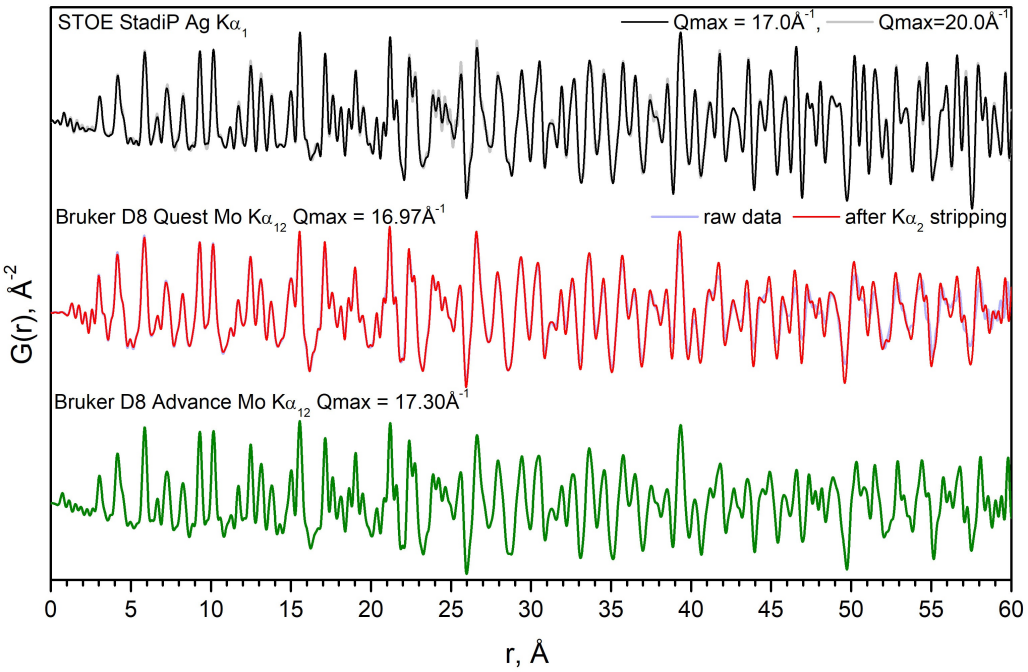

Figure S8 Comparison of experimental PDF of LaB_6 standard acquired on single-crystal Bruker D8 QUEST diffractometer with data processing in original *FormagiX v.0.5* program and two dedicated PDF diffractometers STOE STADI P and Bruker D8 ADVANCE.

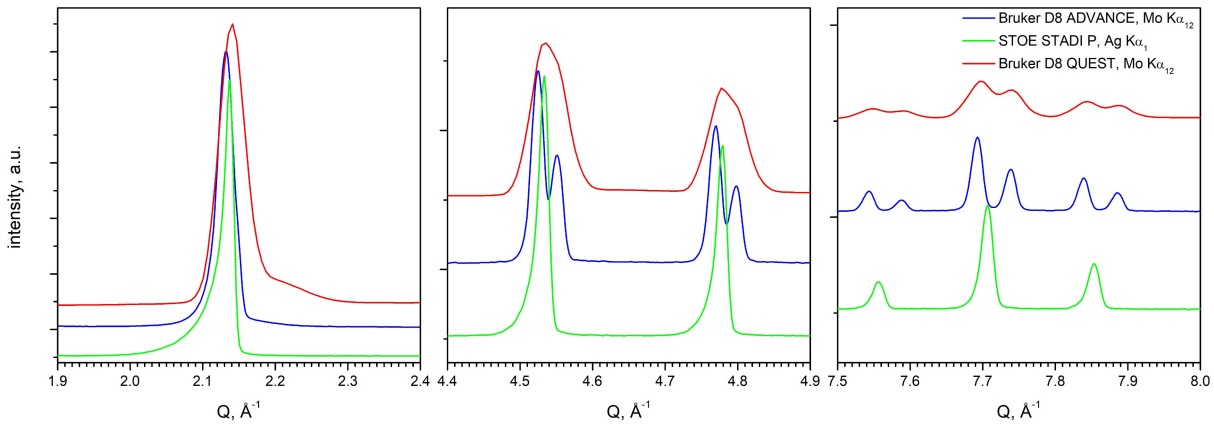

Figure S9 Profiles of total scattering $I(Q)$ of LaB_6 standard collected on Bruker D8 QUEST (Mo $K\alpha_{12}$), Bruker D8 ADVANCE (Mo $K\alpha_{12}$) and STOE STADI P (Ag $K\alpha_{12}$) diffractometers.

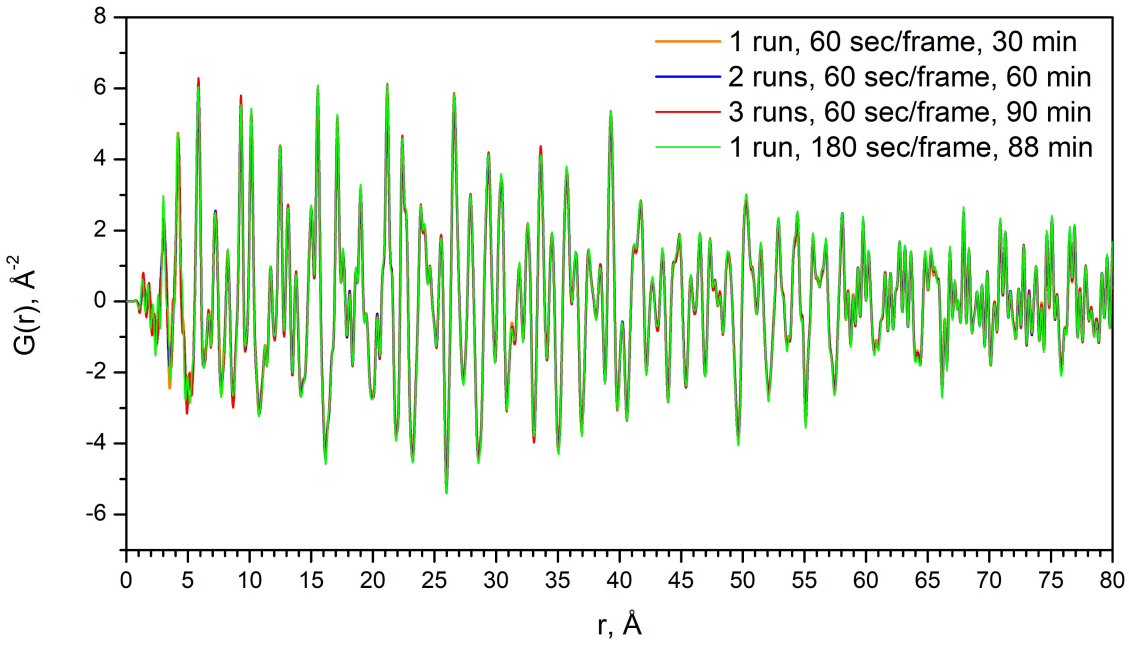

Figure S10 Experimental PDF of LaB_6 standard from total scattering collected on Bruker D8 QUEST with Mo $K\alpha_{12}$ and PHOTON III with different expositions and number of runs. The 25 frames strategy with 100 mm sample-to-detector distance was applied. Frames were integrated with the *FormagiX*. Total scattering data from 2 or 3 runs were summed before generation of PDF.

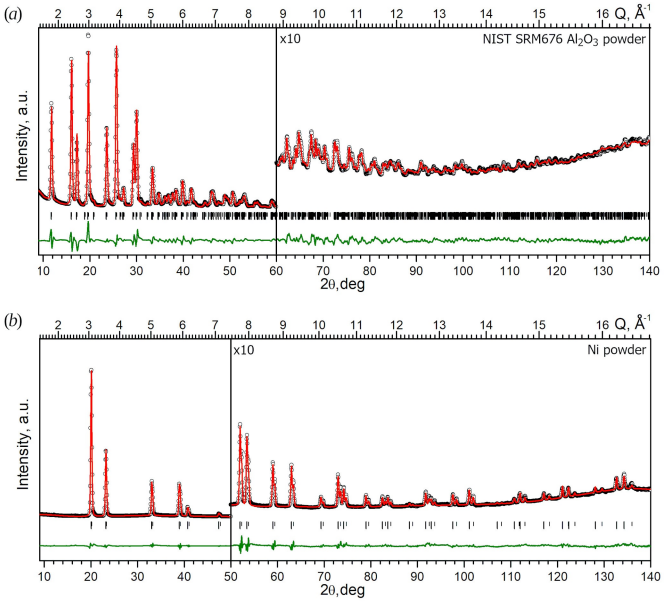

Figure S11 Rietveld refinement plots of NIST SRM676a Al_2O_3 (top) and Ni (bottom) powders collected on Mo Kα_{12} radiation. Experimental data are shown by (◦) markers, red solid lines show calculated profiles, lower green lines show difference profile, vertical bars show calculated Bragg peak positions.

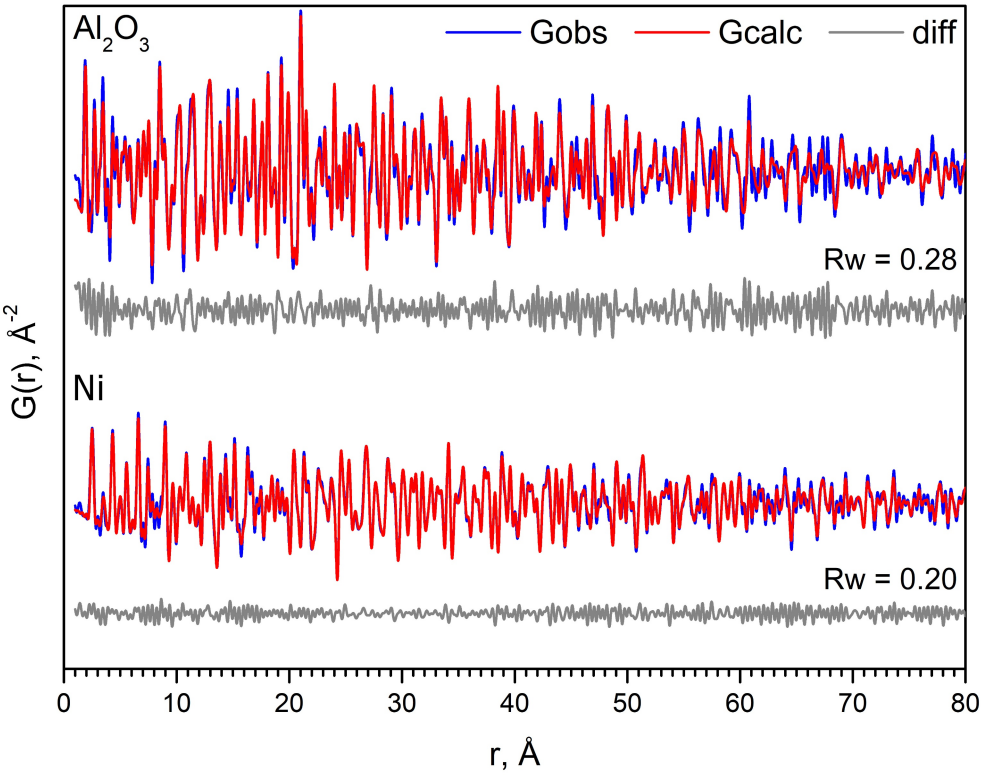

Figure S12 PDF of NIST SMR676 Al_2O_3 (top) and Ni (bottom) powders collected on Mo Kα_{12} radiation for Q_{max}=17 Å^{-1} and their fits by α-Al_2O_3 and fcc-Ni structures respectively.

Table S2 Results of Rietveld and PDF refinement of reference samples.

	NIST SRM676 Al_2O_3				Nickel			
	Rietveld	PDF (1-45Å) Q_{max}=15Å^{-1} Kα$_{12}$	PDF (1-40 Å) Q_{max}=17Å^{-1} Kα$_1$	PDF (1-80 Å) Q_{max}=17Å^{-1} Kα$_1$	Rietveld	PDF (1-45Å) Q_{max}=15Å^{-1} Kα$_{12}$	PDF (1-80Å) Q_{max}=17Å^{-1} Kα$_1$	PDF (1-140Å) Q_{max}=17Å^{-1} Kα$_1$
a, Å	4.7592†	4.7592†	4.7516(9)	4.7527(6)	3.52736(7)	3.5283(9)	3.5255(3)	3.5257(3)
c, Å	12.9918†	12.9918†	12.975(3)	12.974(3)	-	-	-	-
U_{iso}, Å^2	0.0041(2) Al 0.0048(2) O	0.0046(6) Al 0.0091(13) O	0.0040(5) Al 0.0086(12) O	0.0044(4) 0.0097(11)	0.00649(8) Ni	0.0091(12) Ni	0.0085(5) Ni	0.0087(5) Ni
Q_{damp}, Å^{-1}	-	0.018(4)	0.021(3)	0.022(1)	-	0.017(6)	0.020(1)	0.0194(8)
Q_{broad}, Å^{-1}	-	0.037(5)	0.022(6)	0.014(3)	-	0.028(6)	0	0
R_w	0.0348	0.171	0.215	0.282	0.0129	0.0939	0.203	0.233

† - parameters were fixed from the NIST certificate.

S5. Results of PDF analysis of $[Sm_4(OH)_2(piv)_{10}(H_2O)_2]_\infty$ powder

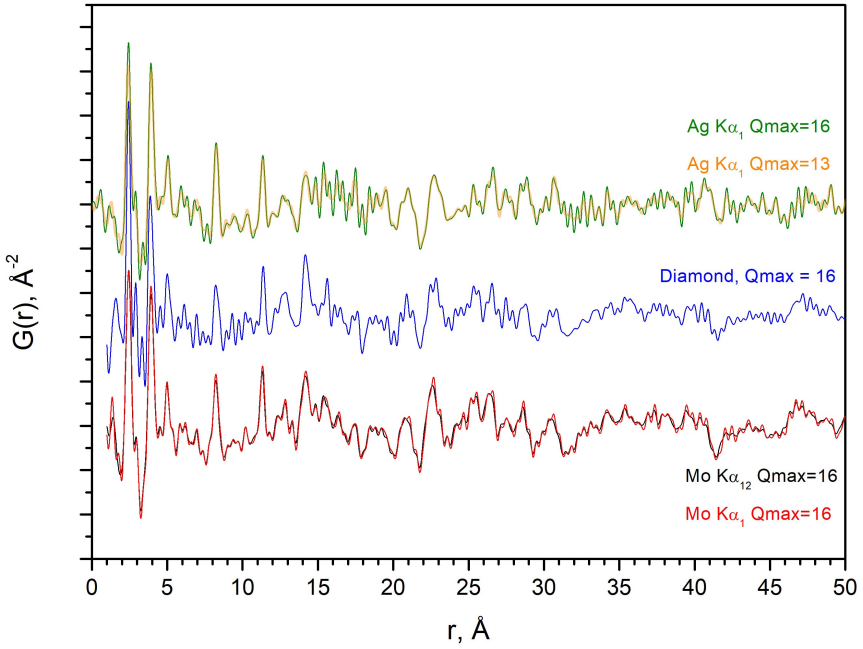

Figure S13 Comparison of experimental PDF for $[Sm_4(OH)_2(piv)_{10}(H_2O)_2]_\infty$ powder acquired on different X-ray sources, namely on two laboratory diffractometers with Ag Kα$_1$ (STOE STADI P) and Mo Kα$_{12}$ (Bruker D8 QUEST), as well as at Diamond Light Source, with Q_{max} = 16 Å^{-1} or 13 Å^{-1}. Mo-PDF was also generated from total scattering data after Kα$_2$ stripping.

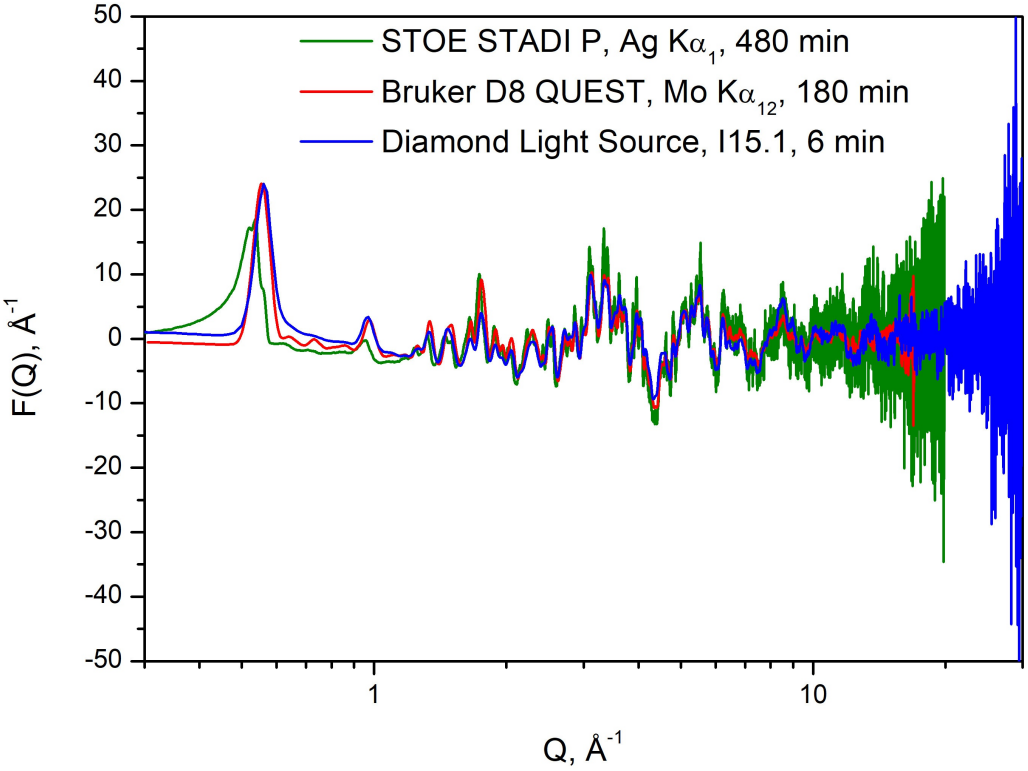

Figure S14 Experimental $F(Q)$ of $[Sm_4(OH)_2(piv)_{10}(H_2O)_2]_\infty$ powder acquired on different instruments: dedicated PDF diffractometer STOE STADI P with Ag $K\alpha_1$ radiation, dedicated PDF I15.1 beamline of Diamond Light Source synchrotron and single crystal diffractometer Bruker D8 QUEST with Mo $K\alpha_{12}$ radiation.

Table S3 Selected interatomic distances within $[Sm_4(OH)_2(piv)_{10}(H_2O)_2]_\infty$ species determined by refinement of experimental PDF (from Bruker D8 QUEST Mo $K\alpha_{12}$ and STOE STADI P Ag $K\alpha_1$) and partial single crystal XRD analysis (Grebenyuk *et al.*, 2021). The DFT optimized structural model derived from model 2 was used for fit of PDF as reported earlier. Symmetry code: (i) 1−*x*, 1−*y*, 2−*z*.

	Bruker D8 QUEST Mo $K\alpha_{12}$ *r* range 1-30 Å Q = 0.3-15 Å^{-1}	STOE STADI P Ag $K\alpha_1$ *r* range 1-30 Å Q = 0.73-13.8 Å^{-1}	Single crystal XRD[3]
Sm1-Sm2	3.88(7)†	3.889(2)†	3.822(5)
Sm1-Sm1^{i}	3.85(5)	3.851(2)	3.839(6)
Sm1^{i}-Sm2	4.03(8)	4.085(2)	4.088(3)
Sm1-O11	2.43(8)	2.4119(17)	2.53(3)
Sm2-O11	2.49(3)	2.5303(12)	2.50(3)
Sm1^{i}-O11	2.33(3)	2.3582(10)	2.25(2)
R_w	28.0	42.0	-

† — note that scale, cell parameters and ADP were refined, while fractional coordinates were fixed in the PDF fits. Therefore, the uncertainties of the interatomic distances presented are derived from the uncertainties of the unit cell parameters only.

S6. Details of total scattering study of $Ln(tfa)_3$+deta+^{i}PrOH solutions

Table S4 Estimated Mo $K\alpha_{12}$ X-ray absorption of solution samples

Sample	μ, mm^{-1}	Capillary radius, mm	μR	Transmittance, %
$La(tfa)_3$+deta+^{i}PrOH	0.171	0.75	0.13	77
$Pr(tfa)_3$+deta+^{i}PrOH	0.190	0.75	0.14	76
$Gd(tfa)_3$+deta+^{i}PrOH	0.240	0.75	0.18	70
$Tb(tfa)_3$+deta+^{i}PrOH	0.252	0.75	0.19	68
$La(tfa)_3$+^{i}PrOH	0.174	0.75	0.13	77
^{i}PrOH	0.034	0.75	0.03	94
deta+^{i}PrOH	0.039	0.75	0.03	94

Absorption coefficients were estimated using the APS Compute X-ray Absorption web instrument (Von Dreele *et al.*, 2013).

Table S5 Position of two major peaks in experimental PDF (Q_{max} = 11 Å^{-1}) of reactive solutions of $Ln(tfa)_3$+deta in isopropanol (Ln = La, Pr, Gd, Tb) compared with Shannon ionic radii for Ln^{3+} for coordination number 9.

Ln	Ln-O, Ln-N	Ln···Ln	Shannon ionic radius, Å
La	2.67	4.07	1.216
Pr	2.65	4.00	1.179
Gd	2.60	3.88	1.107
Tb	2.54	3.80	1.095

Table S6 Interatomic distances (Å) in $[Pr_4(deta)_4(OH)_4(tfa)_3(detadcH)_2]^{3+}$ complex cation in the crystal structure of **Pr$_4$**. Symmetry code (i): 1−*x*, −*y*, 1−*z*.

Parameter	Distance	Parameter	Distance
Pr1–O2	2.462(4)	Pr2–O2^i	2.456(4)
Pr1–O2^i	2.447(3)	Pr2–O8^i	2.476(5)
Pr1–O1	2.470(4)	Pr2–O1^i	2.491(4)
Pr1–O3	2.622(4)	Pr2–O1	2.502(4)
Pr1–O7	2.493(4)	Pr2–O6^i	2.515(4)
Pr1–O9^i	2.477(5)	Pr2–O5^i	2.539(5)
Pr1–N1	2.683(5)	Pr2–N4	2.682(5)
Pr1–N2	2.683(5)	Pr2–N5	2.684(6)
Pr1–N3	2.658(6)	Pr2–N6	2.682(5)
Pr1–Pr1^i	4.0626(5)	Pr2–Pr2^i	4.0277(6)
Pr1–Pr2	3.9340(4)	Pr1–Pr2^i	3.9379(4)

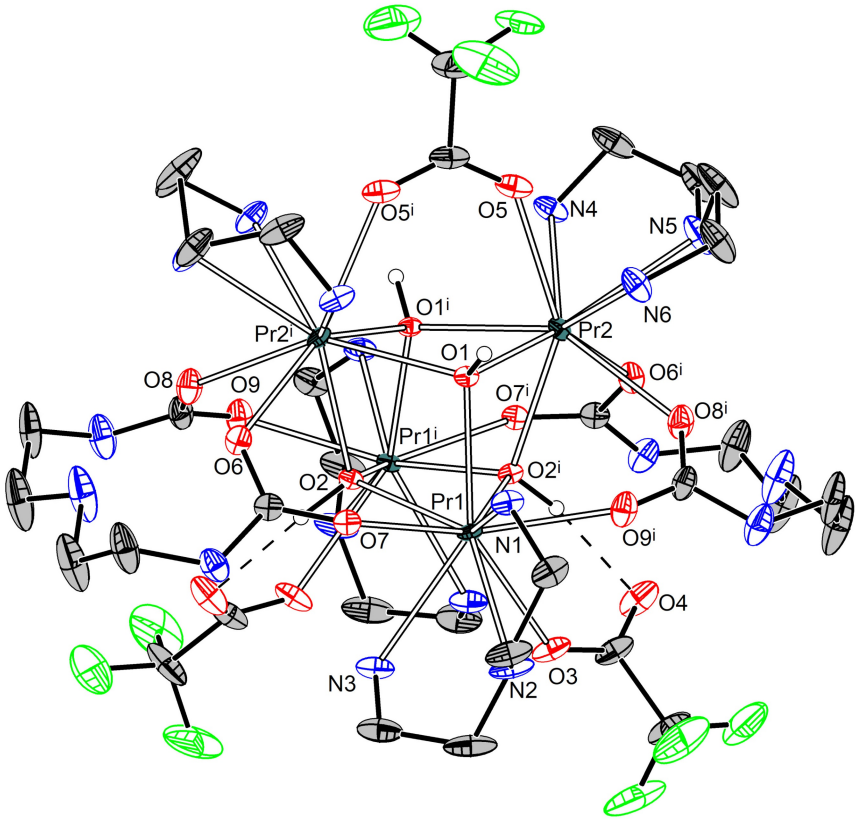

Figure S15 $[Pr_4(deta)_4(OH)_4(tfa)_3(detadcH)_2]^{3+}$ complex cation in **Pr$_4$** crystal structure. Most H atoms are omitted for clarity. Symmetry code (i): $1-x, -y, 1-z$.

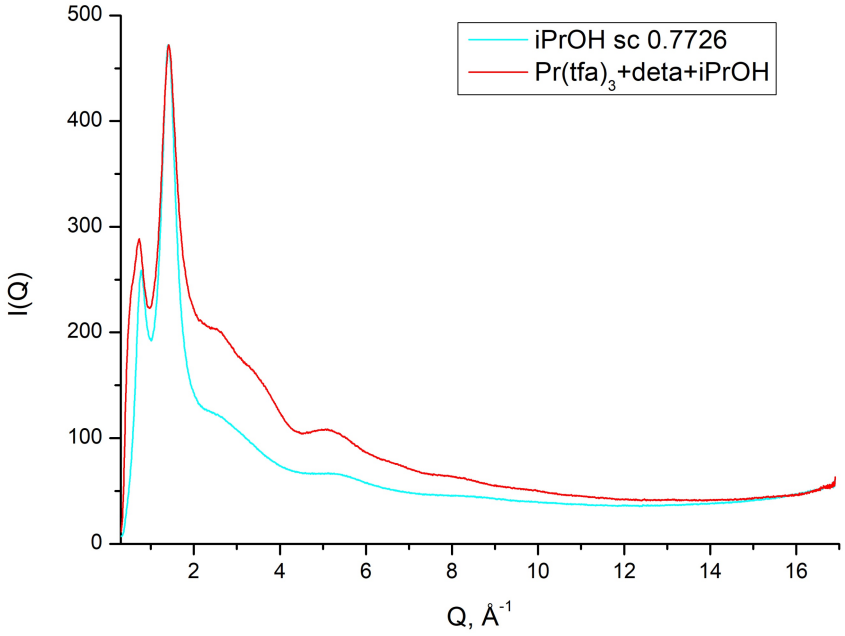

Figure S16 Total scattering data of $Pr(tfa)_3$ + deta + isopropanol solution and blank ^{i}PrOH in Kapton® capillaries. Acquisition time 30 min.

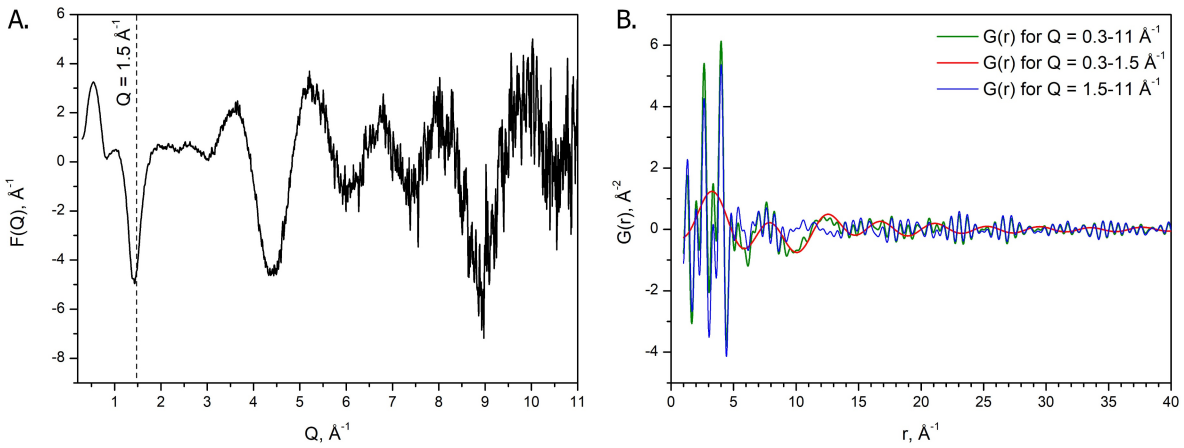

Figure S17 A) Reduced total scattering structure function, $F(Q) = Q[S(Q) - 1]$ of $Pr(tfa)_3$ + deta + isopropanol solution, employing the scattering of isopropanol in Kapton® capillary as background. B) Resulting PDFs of the solution of A for different Q-ranges for Fourier Transformation. The small range of 0.3 – 1.5 Å^{-1} (red curve) shows, that this Q range introduces the sinusoidal oscillation to the PDF data calculated from the entire range of 0.3 - 11 Å^{-1} (green curve).

S7. Experimental part

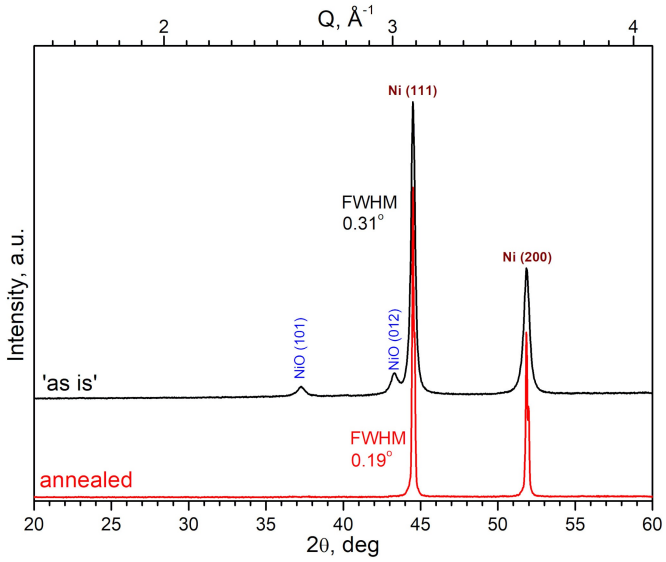

Figure S18 PXRD pattern (Cu Kα, λ = 1.5418Å) of Nickel powder used as reference sample for PDF. Pattern of purchased Carbonyl Nickel 'as is' shows broadened XRD peaks and presence of native NiO admixture. Pattern of nickel powder after annealing at 800ºC for 24h in oxygen-free atmosphere shows no admixture peaks and remarkably improvement of crystallinity.

Table S7 Summary of the crystal structure and refinement details for **Pr_4**.

Parameter	**Pr_4**
Formula	$Pr_4O_{32}C_{42}N_{18}H_{93}F_{21}$
Formula weight	2324.98
Diffractometer	Bruker D8 QUEST
Data collection method	ω scans
Temperature (K)	100(2)
Crystal system	Monoclinic
Space group	C2/c
a (Å)	27.6254(9)
b (Å)	12.7853(4)
c (Å)	23.5496(8)
α (°)	90
β (°)	98.4791(11)
γ (°)	90
V (Å^3)	8226.8(5)
Z	4
Colour, habit	Colourless, needle
Crystal dimensions (mm)	0.230 × 0.205 × 0.139
Density D_{calc} (g·cm^{-3})	1.877
μ (mm^{-1})	2.461
Unique reflections (R_{int})	8987 (0.043)
Observed reflections [$I > 2\sigma(I)$]	7970
Parameters	520
$R_1[I > 2\sigma(I)]$, ωR_2	0.0502, 0.1376
Goodness of fit on F^2	1.034
Absorption correction	SADABS
T_{min}, T_{max}	0.6742, 0.9578
ρ_{min}, ρ_{max} (eÅ^{-3})	-1.323, 2.116

S8. Description of FormagiX v.0.5 software solution for serial frame integration

FormagiX program is the original software solution developed for serial azimuthal integration of Bruker Photon II and Photon III frames to obtain powder XRD pattern $I(2\theta_i)$. The program is written using Free Pascal language within the framework of cross-platform (Linux, Windows, MacOS) Lazarus IDE (Lazarus and Free Pascal Team, 2022). Compiled program binaries are available upon request.

This section presents a brief description of geometrical model, assumptions and algorithms applied in a current version of FormagiX v.0.5. More detailed discussions and fundamentals of 2D XRD data treatment one can find in the recent comprehensive book by Bob B. He (He, 2018).

Reading of Bruker Photon II/III frames by FormagiX program is performed by original parser based on the reported description of Bruker Frame file format (Grüne). Bruker Frame File contains header section with a set of important parameters (among them are wavelengths of X-ray radiation; positions of goniometer axes $2\theta_D$, χ, φ, and ω; exposure time; sample-to-detector distance *DD*; position of detector center *XC* and *YC*) specific for certain frame and pixel matrix with compression which stores number of photons counted by each pixel. Values of parameters read from Frame file are used for constructing of geometrical model for Frame integration.

Geometrical model used in FormagiX

Primary beam passes through the sample at point *O* (goniometer center) and then falls on the detector (Fig. S19). Point C is the point of normal incidence of the beam on the detector (the *OC* line is orthogonal to the detector plane) when the detector is at position with $2\theta_D = 0$. Point C is the true center detector, and it corresponds to the center of Debye rings ($2\theta = 0$). *XC* and *YC* are coordinates of C point counted from the detector corner, the length of *OC* line segment is the sample-to-detector distance *DD*, these are three basic model parameters. Starting values of *XC*, *YC* and *DD* parameters are stored in the Frame Header, but precise integration requires their calibration against standard and should be re-calibrated each time after manual movement of the detector. Position of detector on the 2θ axis - '$2\theta_D$' is also stored in Frame Header, the current version of FormagiX v.0.5 considers this value accurate enough for precise integration and uses it without calibration. Further versions may include correction of detector tilts from roll, pitch and yaw.

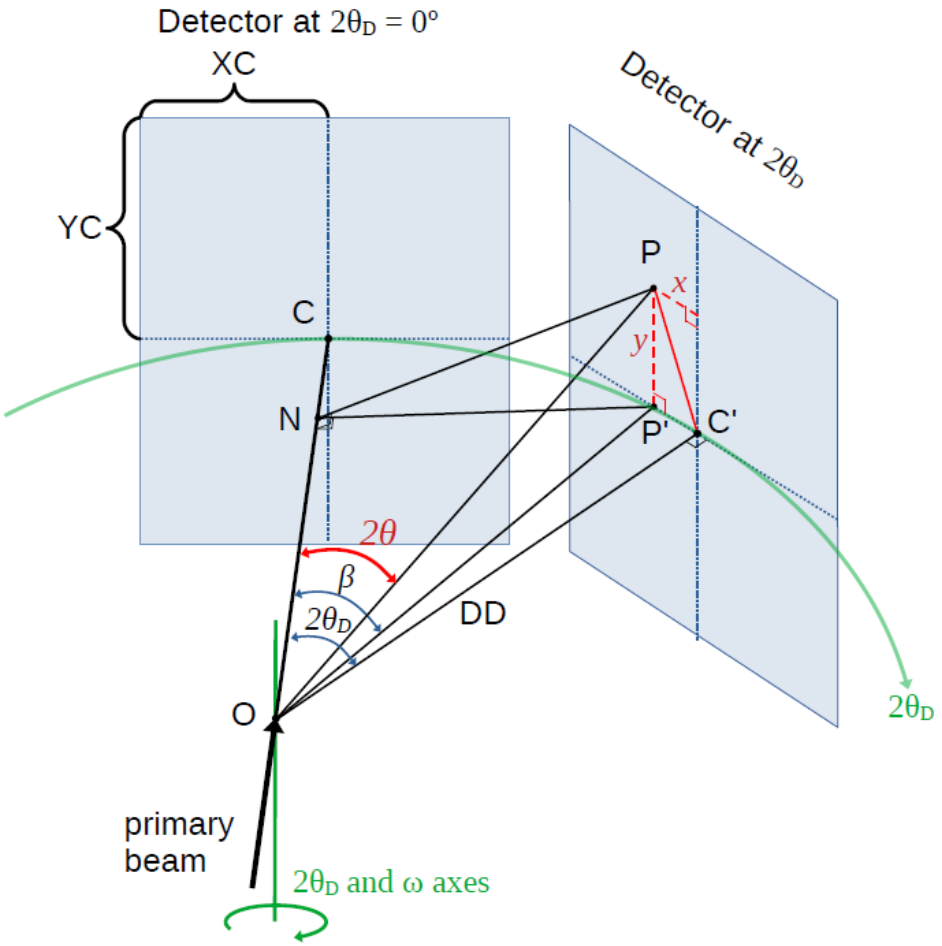

Figure S19 Geometrical model used for frames integration algorithm in FormagiX software.

For each pixel P with certain coordinates X_P and Y_P of pixel center counted from the detector corner the 2θ value can be calculated as follows:

$x = (X_P - XC) \times s$ and $y = (Y_P - YC) \times s$ are coordinates (mm) of pixel P counted from the detector corner, where s is the pixel size (for Photon III detector $s = 0.135$ mm);

C' – is the true center of the detector, equals to C point but for a certain $2\theta_D$ position;

the length OC' line segment, $|OC'|$ is equal to $|OC|$ and to sample-to-detector distance DD;

OP – is the line segment between the sample and pixel of interest P, $|OP|^2 = DD^2 + x^2 + y^2$;

OP' – is the orthogonal projection of OP line segment on the equatorial plane, $|OP'|^2 = DD^2 + x^2$.

The angle between OC and OP' lines displaced in equatorial plane $\angle COP' = \beta = 2\theta_D - \angle P'OC'$,

where $tg(\angle\ P'OC') = \frac{x}{DD}$, so $\beta = 2\theta_D - arctg\frac{x}{DD}$

The line segment *ON* is the orthogonal projection of *OP′* segment on *OC* line and its length equals to $|ON| = |OP'| \cos\beta$.

On the other hand, *ON* is a cathetus of an orthogonal triangle *OPN*, where its length equals to $|ON| = |OP| \cos 2\theta$.

So, 2θ value can be calculated from the equation $|OP| \cos 2\theta = |OP'| \cos\beta$.

After substitution of all expressions for variables the final equation for cos 2θ is

$$\cos 2\theta = \sqrt{\frac{DD^2 + x^2}{DD^2 + x^2 + y^2}} \cdot \cos\left(2\theta_D - arctg\frac{x}{DD}\right) \qquad (3)$$

Therefore, for each pixel within the 1024×768 matrix of Photon III C14 detector the 2θ value of pixel center can be calculated with equation (3).

Conversion of pixel matrix of 2D Frame to $I(2\theta)$ is performed within fixed $\Delta 2\theta$ step, reasonable values of $\Delta 2\theta$ are 0.02 – 0.05º. Thus, the certain pixel P with calculated 2θ value for pixel center contributes the intensity to $I(2\theta_i)$ if 2θ satisfies the conditions $2\theta_i - ½\ \Delta 2\theta < 2\theta \leq 2\theta_i + ½\ \Delta 2\theta$. In other words the counted photons of pixel P is added to $I(2\theta_i)$ if the center of the pixel lies inside a the corresponding band of $\Delta 2\theta$ width with a middle line at $2\theta_i$.

It is worth noting that the Photon III detector has pixel height and width being equal to 0.135 mm. For the sample-to-detector distance of 100 mm the difference between 2θ values for neighbor pixel centers ranges from 0.063 to 0.078° depending on pixel position in matrix and $2\theta_D$ detector position. This step being irregular is remarkably larger than desired integration step $\Delta 2\theta$, as a result photons collected by the whole large area 'natural' pixel attributed to the piece of only one band (e.g. to $2\theta_{i+1}$ band in Figure S20) while neighbor bands which also go across the certain natural pixel receive nothing.

To overcome this issue FormagiX virtually separates each natural pixel into arrays of smaller subpixels. One can vary the proper number subpixels within one natural pixel from 4 (2×2 array) to 25 (2×2 array) since the larger number slows down the integration process. By default settings natural pixel is separated onto 3×3 array that gives the separation between subpixel centers of 0.021 – 0.026º being twice smaller than default integration step of 0.05º. The number of counted photons of natural pixel is considered equally distributed on all of its

subpixels. Similarly to natural pixels, the certain subpixel contributes to $I(2\theta_i)$ if 2θ value of its center satisfies the conditions $2\theta_i - ½\ \Delta 2\theta < 2\theta \leq 2\theta_i + ½\ \Delta 2\theta$. This approach results in more accurate counting (Figure S20).

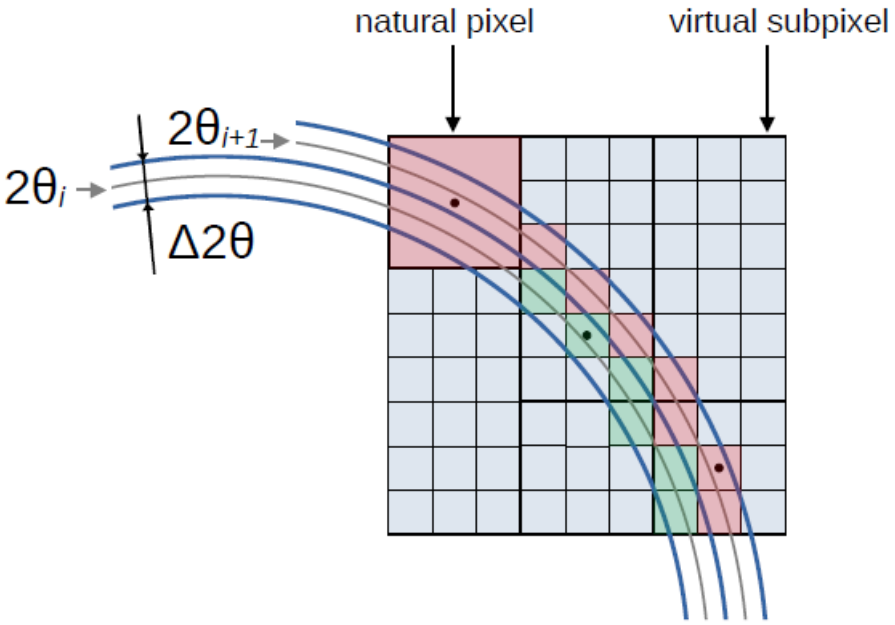

Figure S20 Scheme of pixel attribution to certain 2θ value.

Processing each frame with the above-described algorithm generates fragments of $I(2\theta_i)$ dataset, which consolidation results in $I(2\theta_i)$ for the full range. The equation (4) determines the observed intensity $I(2\theta_i)$ for each $2\theta_i$ value:

$$I\left(2\theta_i\right)=\frac{1}{N\left(2\theta_i\right)}\sum_{j=1}^{N\left(2\theta_i\right)} I_j \cdot norm_j \qquad (4)$$

where $N(2\theta_i)$ is the total number of pixels of all Frames within the series which contribute to $2\theta_i$ band, i.e. which satisfy the condition $2\theta_i - ½\ \Delta 2\theta < 2\theta \leq 2\theta_i + ½\ \Delta 2\theta$;

I_j is the number of photons counted by j^{th} pixel among those which contribute to $2\theta_i$ band;

$norm_j$ is the normalization factor for intensity of j^{th} pixel.

Photon detector has flat active area and as a result different pixels across its surface are displaced at different distances from the sample (point O) and their surfaces despite identical size occupy different solid angles. This affects the number of counted photons per pixel. Namely, pixels near the center of the detector collect the photons from a larger solid angle than pixel which contributes to the same $2\theta_i$ band displaced near the detector corner.

Assuming this, the number of photons counted by different pixels needs a normalization to identical solid angle. Therefore, for a certain pixel with x and y coordinates, the normalization is determined by the equation (5):

$$norm = \left(\frac{\sqrt{DD^2 + x^2 + y^2}}{DD} \right)^3 \tag{5}$$

Calculation of intensities by eq. 4 generates the pattern $I(2\theta_i)$ where each value represents the mean number of photons per pixel within $2\theta_i$ band and regardless the number of pixels of such type. The latter is also stored and is useful for proper estimation of intensity uncertainty $\sigma I(2\theta_i)$.

Calibration of the detector parameters

The integration of 2D frame to obtain $I(2\theta)$ with the above described geometrical model requires the values of three geometrical parameters *XC*, *YC* and *DD*. The initial values of these parameters are stored in the frame header. The precise actual values for *XC*, *YC* and *DD* can be obtained by the refinement against standard powder samples. For this purpose it is necessary to collect one ***calibration frame*** for any standard powder sample, like LaB_6, Si, Al_2O_3 etc. in strictly identical conditions as for samples. In general, it is possible to perform the refinement for frame collected with any $2\theta_D$ detector position, but frame with $2\theta_D = 0$ which cover the angular range of 2θ from –40 to +40º for 100 mm detector distance provides the most robust refinement.

It worth noting that full azimuthal integration of ***calibration frame*** with initial values of *XC*, *YC* and *DD* parameters possibly leads to splitted and shifted peaks on the resulting $I(2\theta)$ profile due to misalignment (Fig. S21). To refine the *XC*, *YC* and *DD* values, the following algorithm is used by FormagiX.

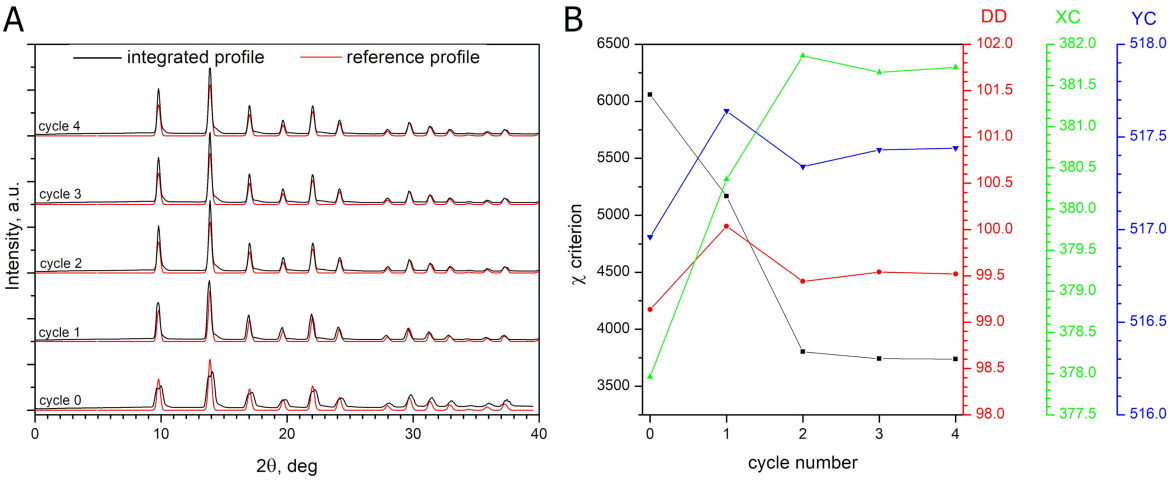

Figure S21 Calibration of detector parameters *DD*, *XC* and *YC* against Frame with $2\theta_D = 0$ for NIST SMR660 LaB_6 powder: A) experimental profile acquired by integration of frame with current parameter for each refinement cycle (cycle 0 corresponds to integration with initial parameters) in comparison with theoretical profile of LaB_6; B) variation of refinement parameters and χ criterion (not to be confused with Euler χ angle) during the refinement.

Firstly, the theoretical powder profile $I_{theo}(2\theta_i)$ of a standard sample is generated based on structural data. The Gaussian profile shape function is used for each peak with constant user-defined FWHM (H) and overall scale factor (S). This approach allows to take into account the presence of $K\alpha_1$ and $K\alpha_2$ doublet in X-ray radiation and to simulate the theoretical profile.

$$I_{theo}(2\theta)=\sum_j \left[S I_j \frac{C_G}{H} e^{\frac{-C_G\left(2\theta-2\arcsin\left(\frac{\lambda_1}{2d_j}\right)\right)^2}{H^2}} + \frac{1}{2} S I_j \frac{C_G}{H} e^{\frac{-C_G\left(2\theta-2\arcsin\left(\frac{\lambda_2}{2d_j}\right)\right)^2}{H^2}} \right] \quad (6)$$

where $C_G = 4 \ln 2$ is a normalization factor;

I_j is the calculated intensity of j-th reflection;

d_j – is the interplanar spacing for j-th reflection;

λ_1 and λ_2 are the wavelengths of $K\alpha_1$ and $K\alpha_2$ peaks.

After that, the integrated profile is compared with theoretical one to calculate the χ criterion:

$$\chi=\sqrt{\sum_i \left(I(2\theta_i)-I_{theo}(2\theta_i)\right)^2} \quad (7)$$

The non-linear least-square refinement of *DD*, *XC*, and *YC* parameters is performed within the coordinate descent method. Each refinement cycle includes sequential change of *DD*, *XC* and *YC* followed by reintegration of the Frame with actual parameters to calculate new value of χ criterion. The optimization of *DD*, *XC*, and *YC* parameters is performed to achieve the minimum of χ criterion. It has been found that the convergence requires 4-10 cycles of refinement depending on the initial values of refined parameters (Fig. S21). The values of refined parameters are appropriate for further integration of other frames with other values of $2\theta_D$ values, indeed the integrated profiles of LaB_6 frames in 2θ ranges of 4–61º, 44–96º and 93–146º perfectly fit theoretical ones (Fig. S22).

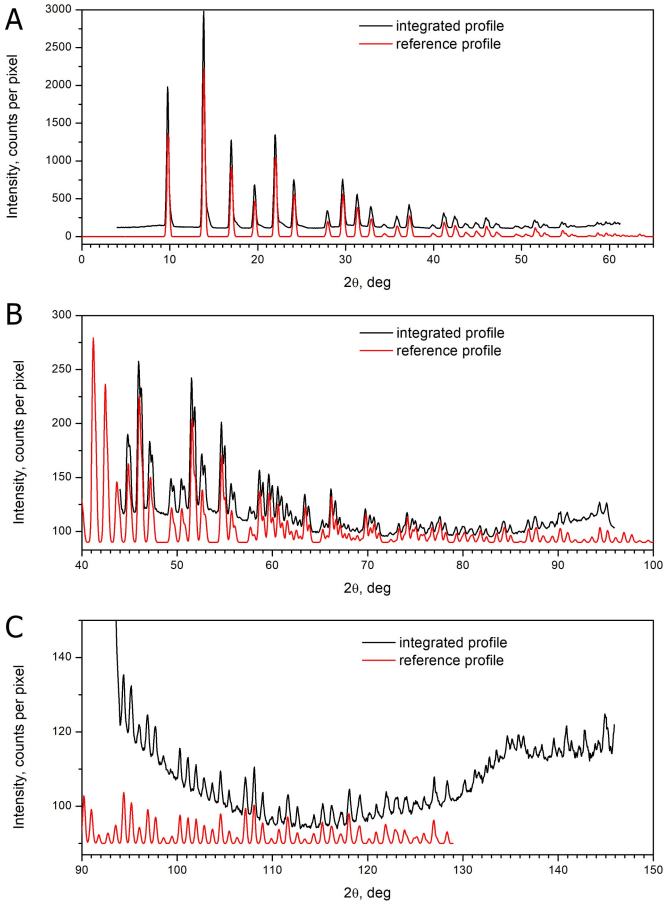

Figure S22 Experimental profile of LaB_6 powder acquired by integration of frames with detector position $2\theta_D$ equals to 30º (A), 70º (B) and 120º (C). The *DD*, *XC* and *YC* parameters for integration were obtained by refinement against single frame with $2\theta_D = 0°$. Position and intensity of peaks on integrated profiles are in a good agreement with the reference profiles for LaB_6 powder. The constant background, a signal of 90 counts per pixel was added to the reference profile in panels B and C to make comparison easier. Note the peak splitting on integrated profile in 45-65° originates from $K\alpha_1$ and $K\alpha_2$ doublet of X-ray radiation. It is also simulated in the reference profile, yet a stronger overlap of simulated peaks occurs due to slightly overestimated FWHM parameter.

References

Farrow, C. L. & Billinge, S. J. L. (2009). *Acta Crystallogr A Found Crystallogr*. **65**, 232–239.

Grebenyuk, D., Zobel, M., Polentarutti, M., Ungur, L., Kendin, M., Zakharov, K., Degtyarenko, P., Vasiliev, A. & Tsymbarenko, D. (2021). *Inorganic Chemistry*. **60**, 8049–8061.

Grüne, T. sfrmtools. https://homepage.univie.ac.at/tim.gruene/research/programs/conv/sfrmtools/

He, B. B. (2018). Two-dimensional X-ray diffraction Hoboken, NJ: John Wiley & Sons.

Lazarus and Free Pascal Team. (2022). https://www.lazarus-ide.org/

Von Dreele R. B., Suchomel M. R. & Toby B. H. (2013). Compute X-ray Absorption. Advanced Photon Source. https://11bm.xray.aps.anl.gov/absorb/absorb.php

Warren, B. E. (1990). X-Ray Diffraction (Dover Books on Physics) Dover Publications.